Effect of Au Nanorods on Potential Barrier Modulation in Morphologically Controlled Au@Cu₂O Core−Shell Nanoreactors for Gas Sensor Applications

Sanjit Manohar Majhi,[†] Prabhakar Rai,[‡] Sudarsan Raj,[†] Bum-Soo Chon,[†] Kyung-Kuen Park,[†] and Yeon-Tae Yu*,[†]

[†]Division of Advanced Materials Engineering and Research Centre for Advanced Materials Development, College of Engineering, Chonbuk National University, Jeonju 561-756, South Korea

[‡]Department of Materials Science and Engineering, Korea University, Seoul 136-701, South Korea

Ⓢ Supporting Information

ABSTRACT: In this work, Au@Cu₂O core−shell nanoparticles (NPs) were synthesized by simple solution route and applied for CO sensing applications. Au@Cu₂O core−shell NPs were formed by the deposition of 30−60 nm Cu₂O shell layer on Au nanorods (NRs) having 10−15 nm width and 40−60 nm length. The morphology of Au@Cu₂O core−shell NPs was tuned from brick to spherical shape by tuning the pH of the solution. In the absence of Au NRs, cubelike Cu₂O NPs having ∼200 nm diameters were formed. The sensor having Au@Cu₂O core−shell layer exhibited higher CO sensitivity compared to bare Cu₂O NPs layer. Tuning of morphology of Au@Cu₂O core−shell NPs from brick to spherical shape significantly lowered the air resistance. Transition from p- to n-type response was observed for all devices below 150 °C. It was demonstrated that performance of sensor depends not only on the electronic sensitization of Au NRs but also on the morphology of the Au@Cu₂O core−shell NPs.

KEYWORDS: Au@Cu₂O, core−shell nanoparticles, depletion layers, gas sensors, CO
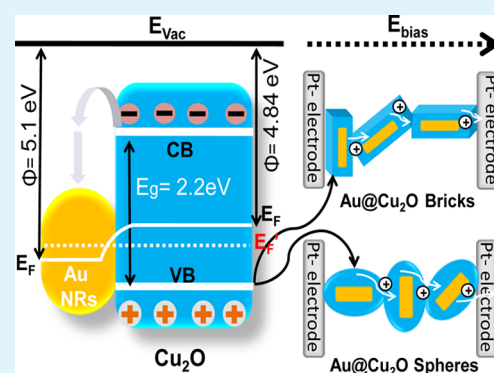
INTRODUCTION

The fabrication of multifunctional hybrid nanostructures with unique physicochemical properties has received immense research interest for researchers and scientists in the recent era of nanoscience and nanotechnology.[1−3] In this regard, noble metal NPs and semiconductor oxides have played an important role in designing various hetero systems for many practical applications.[4−8] Among them, a great deal of attention has been given to sensor for the detection of various harmful gases and volatile organic compounds (VOCs) owing to the growing environmental problems and human safety issues. In particular, metal oxide semiconductors (MOS) are considered as widely studied gas sensing materials, over the past few decades.[9−12] A general gas sensing mechanism of a MOS is the charge transfer between adsorbed oxygen molecules and MOS leads to the formation of a space charge region on the surface of MOS, and thus increase or decrease of electrical resistance of the semiconductors upon exposure to oxidizing and reducing gases.[9,13]

However, the continuing need for novel gas sensors with high sensitivity, lower operating temperature, and long-term stability compared to conventional gas sensing devices, drives new developments in the gas sensing field. As a result, several considerable effort has been devoted in order to circumvent the above practical application requirements. One of the effective

way is the incorporation of noble metal NPs onto the semiconductor surface for increasing the performance of gas sensor.[14−16] It is proposed that metal NPs increases the depletion layer formation in metal oxide due to their catalytic activity (chemical as well as electronic sensitization), which increases the sensor response. These noble metal catalysts also function as receptor for the target gas molecules. However, the practice of surface decoration by metal NPs onto MOS are limited at high temperature as metal NPs loss their catalytic activity due to the coagulation of the metal NPs on the support.[17] In addition, noble metals NPs can be poisoned by many chemicals that contain sulfur (H₂S, SO₂, thiols) or phosphorus.[18] Therefore, the development of an efficient and new gas sensor to overcome such problems is necessary.

Moreover, the strategy to fabricate novel high sensitive sensor in a simpler and cost-effective way has remained a challenging task. Recently, the strategy to utilize metal and semiconductor as core−shell hybrid structure for gas sensing application have attracted much attention.[19−23] The core−shell heterostructures shows multifunctional properties, which are different from those of single components. The important fact

about the metal core−semiconductor shell structures is mobile electron can be trapped by the core for a long time due to a large difference between the Fermi energy level of core and semiconductor conduction band energy.[24] Also, the shell layer prevents the aggregation and grain growth of core at high temperature and supports the formation of semiconductor shell layer.[21,25] Apart from the use of noble metals as catalyst, the morphology of sensing material also affects the gas sensor performance as it is related to the carrier transport property of sensing layer (transducer function).[10,26−28] However, very limited work has been done in this area. Therefore, in this study it is emphasized on the morphology dependent gas sensor performance as well as the investigation of effect of noble metal catalyst on gas sensor performance.

Cuprous oxide (Cu_2O) with a direct band gap of about 2.2 eV, has recognized as the most sought-after material due to its many potential applications.[29−32] In spite of so many handful reports on Cu_2O, only few reports are available on its gas sensing properties.[33−35] The most fascinating feature of Cu_2O is that its shape and size can be tuned up by judicious control of reaction conditions.[36] In this work, we have developed a facile method for synthesis of Au@Cu_2O core−shell nanostructures for CO sensing applications. The role of noble metal (Au NRs) on gas sensing properties is investigated by comparing the response of Au@Cu_2O core−shell NPs with bare Cu_2O NPs. Furthermore, the Au@Cu_2O core−shell morphology was tuned by changing the pH of the solution, and hence the effect of morphology on gas sensing properties is also investigated. The underlaying gas sensing mechanism of Au@Cu_2O core−shell nanostructures toward CO gas has been discussed in details. The results demonstrate that sensitivity of gas sensor significantly depends on electronic sensitization of Au NRs as well as morphology of Au@Cu_2O core−shell NPs.

■ EXPERIMENTAL DETAILS

Chemicals and Materials. Hexadecyltrimethylammonium bromide (CTAB; 99%) was purchased from Acros, Morris Plains, NJ. Copper(II) chloride dihydrate ($CuCl_2 \cdot 2H_2O$, 97.5%) was purchased from Shinyo Pure Chemicals Co. Ltd., Japan. Sodium dodecyl sulfate (SDS, 99%) was purchased from Samchun Pure Chemical Co. Ltd., Korea. Sodium hydroxide (NaOH, 93%), Chloroauric acid ($HAuCl_4 \cdot 4H_2O$, 99%) and sodium borohydrate ($NaBH_4$, 98.5%) were purchased from Showa Chemicals Co. Ltd., Japan. Silver nitrate ($AgNO_3$, 99%) was purchased from Sigma-Aldrich. Hydroxylamine hydrochloride ($NH_2OH \cdot HCl$, 99%) acquired from TCL, Japan. All chemicals were analytical grade reagents and used as received without further purification. Milli-Q water (resistivity 18.2 MΩ·cm at 25 °C) was used in all experiments. All glassware was washed with aqua regia, rinsed with water, sonicated 3-fold for 3 min with Milli-Q water and dried before use.

Synthesis of Au NRs. Au NRs were prepared using a typical seed-mediated growth approach reported elsewhere with modification.[37] A gold seed solution was first prepared by adding 0.25 mL of 0.01 M $HAuCl_4$ to 9.75 mL of 0.1 M CTAB solution, and then 0.6 mL of freshly prepared ice-cold 0.01 M $NaBH_4$ solution was quickly added with vigorous stirring for 5 min. Immediately the resulting solution turned to brownish yellow color which was kept at room temperature for 2 h undisturbed to be used as seed solution. For seed mediated growth, a 100 mL volume of growth solution was prepared, 5 mL of 0.01 M $HAuCl_4$ was added to 95 mL of 0.1 M CTAB solution, followed by 0.8 mL of 0.01 M $AgNO_3$ solution with gentle mixing to control the growth of Au NRs. Then 0.55 mL of 0.1 M ascorbic acid was added drop by drop with vigorous stirring. The solution became colorless after ascorbic acid addition. Finally, 120 μL of seed solution was added to initiate the growth. The color of the solution gradually changed within 5−10 min. The reaction mixture was left undisturbed

overnight for longitudinal overgrowth. The as prepared Au NRs solution was centrifuged at 12 000 rpm for 10 min and washed several times to remove unreacted CTAB ions. The final precipitate was dispersed in 25 mL of water for further use.

Synthesis of Au NRs@Cu_2O Core−Shell NPs. The fabrication of Au@Cu_2O core−shell NPs follows previously reported procedure with some modification.[38] In a typical synthesis of the Au@Cu_2O core−shell, 0.117 g of SDS was first dissolved in DI water followed by the addition of 1 mL of $CuCl_2$ solution (0.1 M) with stirring. Then 3 mL of as prepared Au NRs solution was added to the $CuCl_2$−SDS mixture solution followed by the addition of 0.22−0.30 mL of NaOH (1 M) solution with stirring. Finally, 0.25 mL of $NH_2OH \cdot HCl$ (0.1 M) was added with vigorous stirring. Immediately the solution color was changed to yellowish-green. The resulting solution was aged for 2 h with stirring. After 2 h, the reaction was stopped and the solution was centrifuged at 3500 rpm for 10 min with DI water and ethanol to remove excess ions and surfactants for several times. The bare Cu_2O NPs were prepared following the same process without addition of Au NRs into the solution.

Characterization. Powder X-ray diffraction (XRD) patterns of the sample were recorded on a D/Max 2005 Rigaku X-ray diffractometer equipped with graphite manochromatized high intensity Cu Kα (λ = 1.54178 Å). The transmission electron microscope (TEM) images were taken with a JEM-2010 JEOL instrument, whereas high-resolution TEM (HRTEM) and scanning transmission electron microscope (HAADF-STEM) images were taken with a Zeiss EM 912 Omega instrument. Field emission scanning electron microscope (FESEM) images were taken with a Zeiss Supra 40VP instrument. The UV−visible spectra were conducted on a UV−visible spectroscope (UV-2550, Shimadzu).

Gas Sensing Measurements. The gas sensors were fabricated with as synthesized Au@Cu_2O core−shell NPs as sensing materials. To measure the sensor response of the for CO gas, a sensor device was prepared as follows:[19] the synthesized colloid (1 mL) was dropped onto the cleaned Al_2O_3 board (15 mm × 15 mm) with interdigited platinum electrodes (10 mm × 10 mm) and the colloid was dried on a hot plate. The Au@Cu_2O core−shell NPs loaded device was heat treated at 300 °C in a muffle furnace for 5 h. The change in resistance of the device due to the presence of CO was measured using a high resistance meter (Aligent 34970A). The device was examined in the temperature range of 50−250 °C at various concentrations of CO (10−1000 ppm) in a temperature controlled environment. The background gas was N_2 and dry air was mixed to be 10.5% of oxygen. The gas flow rate (100 $cm^3 \cdot min^{-1}$) over the sensor device was switched between the sample gas and dry air to record the sensor response in electrical resistance. The sensor response (R_s) was calculated using R_g/R_a for CO gas. Here R_a is the resistance in dry air and R_g is the resistance in the target gas.

■ RESULTS AND DISCUSSION

The TEM images of Au NRs prepared by the seed mediated method are displayed in Figure 1a. It shows the formation of well dispersed Au NRs with a uniform length and width of 40−
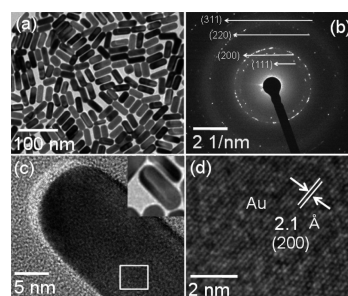
Figure 1. TEM analysis of Au NRs: (a) TEM, (b) SAED, and (c and d) HRTEM of selected Au NRs.

60 and 10−15 nm, respectively. The selected area electron diffraction (SAED) pattern shows ring pattern, which confirms the formation of crystalline structure of Au NRs (Figure 1b). The single crystalline nature of these Au NRs are confirmed from HRTEM analysis, which shows clear lattice fringes as shown in Figures 1c and d. The lattice spacing of 2.21 Å corresponds to (200) plane of Au crystals which reveals that these Au NRs are preferentially grew along [200] direction (Figure 1d).

The formation of Au@Cu$_2$O core−shell NPs is shown in Figure 2. The typical core−shell structure with a brick like
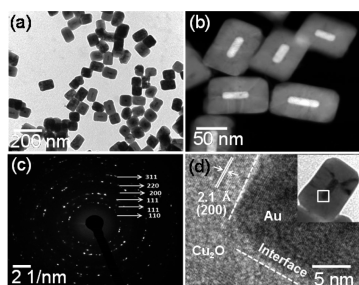
Figure 2. Au@Cu$_2$O core−shell NPs: (a) TEM, (b) HAADF- STEM, (c) SAED, and (d) HRTEM of selected Au@Cu$_2$O core−shell NPs.

structure having Au NRs in the center is obtained, indicating the successful coating of Cu$_2$O NPs over Au NRs (Figure 2a). The length and width of these Au@Cu$_2$O core−shell NPs are 120 ± 10 and 50 ± 5 nm, respectively, whereas Cu$_2$O shell thickness is around 40 ± 5 nm. High-angle annular dark field scanning transmission electron microscopy (HAADF-STEM) images were taken to further confirm the formation of core−shell structure (Figure 2b). It is clear from the image that all the Au@Cu$_2$O core−shell NPs encapsulate only one Au NR and almost no particles with multiple cores or without Au core are found. Figure 2c shows the SAED pattern of individual Au@ Cu$_2$O core−shell NPs shown in inset of Figure 2d, which indicates the polycrystalline nature of the Cu$_2$O shell and consisted of cubic-phase Cu$_2$O nanocrystallites with different orientations. The concentric diffraction rings from inside to outside in Figure 2c are indexed to the (110), (111), (200), (220), and (311) planes of pure cubic phase of Cu$_2$O, respectively, which is in agreement with the XRD results (Figure S1, see the Supporting Information). Figure 2d is the enlarged HRTEM image of the single core−shell NPs, demonstrates that the interplanar spacing of 2.1 Å agrees with the spacing of the (200) lattice plane of Cu$_2$O. This interplanar spacing of Cu$_2$O NPs well match with interplanar spacing of Au NR (2.1 Å), which indicates that there is strong interaction between Au and Cu$_2$O crystals. The {111} planes of Au guide the epitaxial formation of {111} facets of Cu$_2$O, and the [200] direction of Au is parallel to that of Cu$_2$O. Therefore, brick shape Au@Cu$_2$O core−shell NPs is formed.

Figure 3a, is the TEM image of Au@Cu$_2$O core−shell NPs obtained, when NaOH amount was reduced from 0.30 to 0.22 mL. It shows the formation of spherical shape Au@Cu$_2$O core−shell NPs. The inset shows the high magnification TEM image of a single particle of such core−shell NPs. The overall size of Au@Cu$_2$O core−shell NPs ranges from 100 ± 10 nm. Figure 3b displays the HAADF-STEM image of as prepared Au@Cu$_2$O core−shell NPs, which further confirms the formation of core−shell NPs. Compared to bricks like Au@
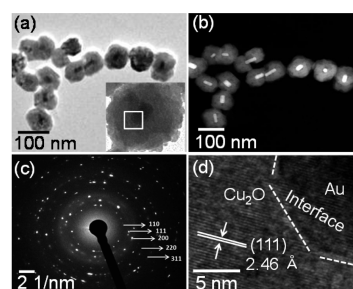
Figure 3. TEM analysis of Au@Cu$_2$O core−shell NPs: (a) TEM, (b) HAADF-STEM, (c) SAED, and (d) HRTEM of selected Au@Cu$_2$O core−shell NPs (inset).

Cu$_2$O core−shell NPs, the shell of these spherical Au@Cu$_2$O core−shell NPs is composed of tinny Cu$_2$O NPs. Figure 3c is the SAED pattern of a single particle (inset Figure 3a), which shows the polycrystalline nature of Cu$_2$O with different orientations starting from inner side of concentric ring to the outside are consist of (110), (111), (200), (220) and (311) which matches with XRD results (Figure S1, see the Supporting Information). Figure 3d is the HRTEM image of a single particle (inset Figure 3a). The interplannar spacing of 2.46 Å corresponds to the (111) plane Cu$_2$O shell. A lattice mismatch of 0.36 Å between Au crystal and Cu$_2$O crystal indicates a weaker interaction between them compared to brick shape Au@Cu$_2$O core−shell NPs.

Figure 4 shows the formation of bare Cu$_2$O cubic NPs without taking Au NRs in the reaction medium. The TEM
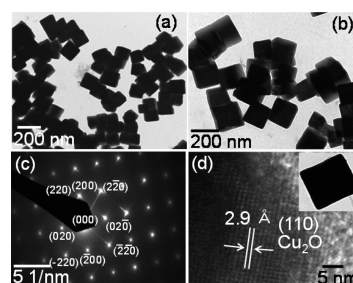
Figure 4. TEM analysis of Cu$_2$O NPs: (a and b) TEM, (c) SAED, and (d) HRTEM of selected Cu$_2$O NPs (inset).

images reveals the formation of cubic shape Cu$_2$O NPs with particle size around 150−200 nm (Figure 4a and b). Figure 4c is the SAED pattern of single particle shown in inset of Figure 4d and exhibits uniform and regular bright spots, which confirms that these nanocubes are single crystalline in nature. The spots are related to the (200) and (220) planes are indexed to the cubic phase of single crystalline Cu$_2$O, which is consistent with XRD pattern (Figure S1, see the Supporting Information). The HRTEM image is shown in Figure 4d, which shows that lattice fringes are distance at 2.9 Å, which is in good agreement with the d value of (110) plane of Cu$_2$O.

Thus, two different types of Au@Cu$_2$O core−shell structures, such as brick and spherical shape, were obtained by changing the amount of NaOH from 0.22 to 0.30 mL. The cubic shape bare Cu$_2$O NPs and brick shape Au@Cu$_2$O shape core−shell NPs were prepared using 0.30 mL of NaOH (pH ~ 12.1). However, spherical shape Au@Cu$_2$O core−shell NPs was formed with addition of 0.22 mL of NaOH (pH ~ 11.5).

XRD analysis was employed to investigate the crystal phase of bare Cu_2O cubic NPs and $Au@Cu_2O$ core–shell heterostructures. As shown in Figure S1 (see the Supporting Information), all the diffraction patterns can be indexed according to cubic phase Cu_2O (JCPDS file No.05-0667). The XRD pattern of as prepared core–shell heterostructures shows strong Cu_2O diffraction peaks and weak diffraction peaks of face centered cubic (fcc) metallic Au (JCPDS No.98–000–0230). No extra peaks of impurities are found in the XRD pattern, which indicates the high purity of synthesized samples.

The optical characterizations of the as-obtained Au NRs, Cu_2O, and $Au@Cu_2O$ core–shell NPs is carried out by the UV–visible absorption spectrum which was demonstrated in Figure S2 (see the Supporting Information). As shown in Figure S2, the surface plasmon (SP) band of Au NRs is recorded at 520 and 690 nm. After the formation of core–shell NPs the SP band of Au NRs is disappeared and only the characteristic absorption feature of Cu_2O occurs.[38] The Cu_2O characteristic absorption peak for brick shape and spherical shape $Au@Cu_2O$ core–shell NPs is recorded at 480 and 457 nm, respectively. The absorption peak of bare Cu_2O cubic NPs is found at around 440 nm. Furthermore, a broad scattering band (480–800 nm) dominates in the absorption spectra of Cu_2O NPs due to large particle size of Cu_2O NPs.[39] The red-shift in absorption peak of Cu_2O after core–shell formation is attributed to the modification of electronic states due to a heterojunction-induced charge transfer interaction.

To demonstrate the potential application of the as prepared $Au@Cu_2O$ core–shell NPs in a gas sensor, we have examined their CO sensing properties. Also the advantage of using Au NRs in $Au@Cu_2O$ core–shell NPs is examined by comparing their response with bare Cu_2O NPs. Figure 5a presents the sensing performance toward CO at 250 °C based on the three

Figure 5. Response transient of as prepared sensing device at different temperatures: (a) 250 °C and (b) 50 °C.

types Cu_2O NPs. It typically shows the p-type semiconducting behavior and resistance increases after introduction of CO gas and reaches a saturation stage. Once, the supply of CO gas is stopped, the resistance decreases again and returns to its original value. These results show that the baseline resistance of brick $Au@Cu_2O$ core–shell NPs is relatively low as compared to cubic Cu_2O NPs, whereas spherical $Au@Cu_2O$ core–shell NPs has lowest. Both types of $Au@Cu_2O$ core–shell NPs are showing better sensing capability compared to bare Cu_2O NPs. Furthermore, the response of $Au@Cu_2O$ bricks is higher than that of spherical $Au@Cu_2O$ core–shell NPs. For example, the response of bare Cu_2O for 1000 ppm of CO gas is 3.35, whereas the response of brick and spherical $Au@Cu_2O$ core–shell NPs is 5.67 and 4.38, respectively. Even for 10 ppm of CO gas, $Au@Cu_2O$ core–shell NPs shows response 1.59 (bricks) and 1.21 (spheres), whereas no response is recorded for bare Cu_2O NPs. For all devices, response increases with increasing gas concentration. However, below 200 °C, no response is recorded below 200 ppm of CO in all devices. Furthermore, reproducibility is checked by three times repeating the response for 1000 ppm of CO and all device exhibit fair reproducibility. Thus, the sensor fabricated from $Au@Cu_2O$ core–shell NPs exhibits a detection limit of 10 ppm and higher sensitivity compared with those obtained by bare Cu_2O NPs. It is found that, below 200 °C, the response for CO gas is switched from p to n-type for bare Cu_2O NPs, whereas similar phenomenon occurred below 150 °C for brick and spherical shape $Au@Cu_2O$ core–shell NPs (Figure S3, see the Supporting Information). It is also found that below 200 °C the baseline resistance of brick $Au@Cu_2O$ core–shell NPs is higher than bare Cu_2O NPs. However, the baseline resistance of spherical $Au@Cu_2O$ core–shell NPs is always lower than other two devices at every temperature. Also, the baseline resistance sharply decreases with increasing temperature (Figure S3d, see the Supporting Information).

Furthermore, the effect of testing temperatures and gas concentrations on sensing behavior of these devices is also examined and illustrated in Figure 6. The response increases with gas concentration in all devices at every temperatures. The response also increases with increasing temperature for these devices, however, no clear trend is recorded from 100 to 150 °C due to transition of response from n- to p-type. Meanwhile, response of both types of $Au@Cu_2O$ core–shell NPs is higher compared to bare Cu_2O at every temperature for every concentration of CO except 150 °C, where the response of brick shape $Au@Cu_2O$ core–shell NPs is lower than that of bare Cu_2O. However, the response of brick shape $Au@Cu_2O$ core–shell NPs is higher than that of spherical $Au@Cu_2O$ core–shell NPs only at 50 and 250 °C, whereas that of spherical one is higher at other temperatures (Figure S4, see the Supporting Information). Furthermore, sensitivity (slope between R_s and concentration) of these samples can be compared by comparing the slope of a calibration graph in Figure 6a–c. It shows that brick shape $Au@Cu_2O$ core–shell layer exhibits a higher sensitivity and better dynamics behavior toward CO than that of bare Cu_2O NPs layer as shown in Figure 6d. Thus, the above results demonstrate that introduction of Au NPs as a core in Cu_2O system improves its sensing performance in terms of slightly higher sensitivity, response time, recovery time and also lowered the operating temperature.

The operating principles of p-type transition metal oxide gas sensors are based on change of sensor conductivity by
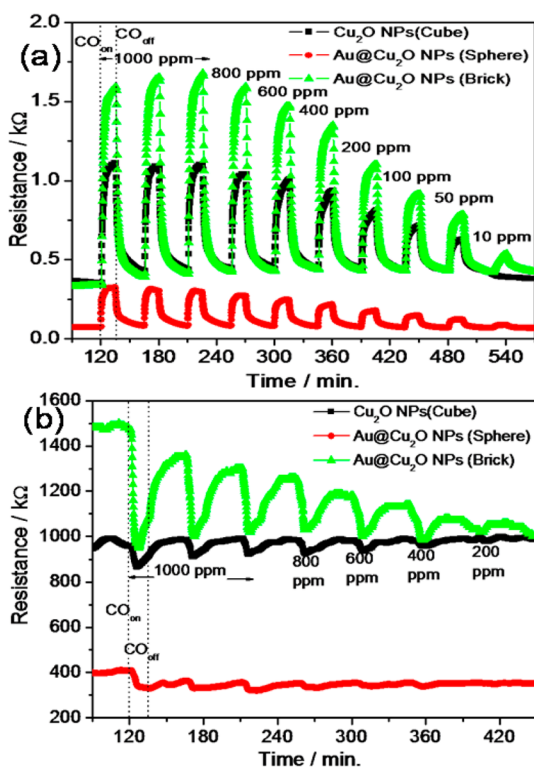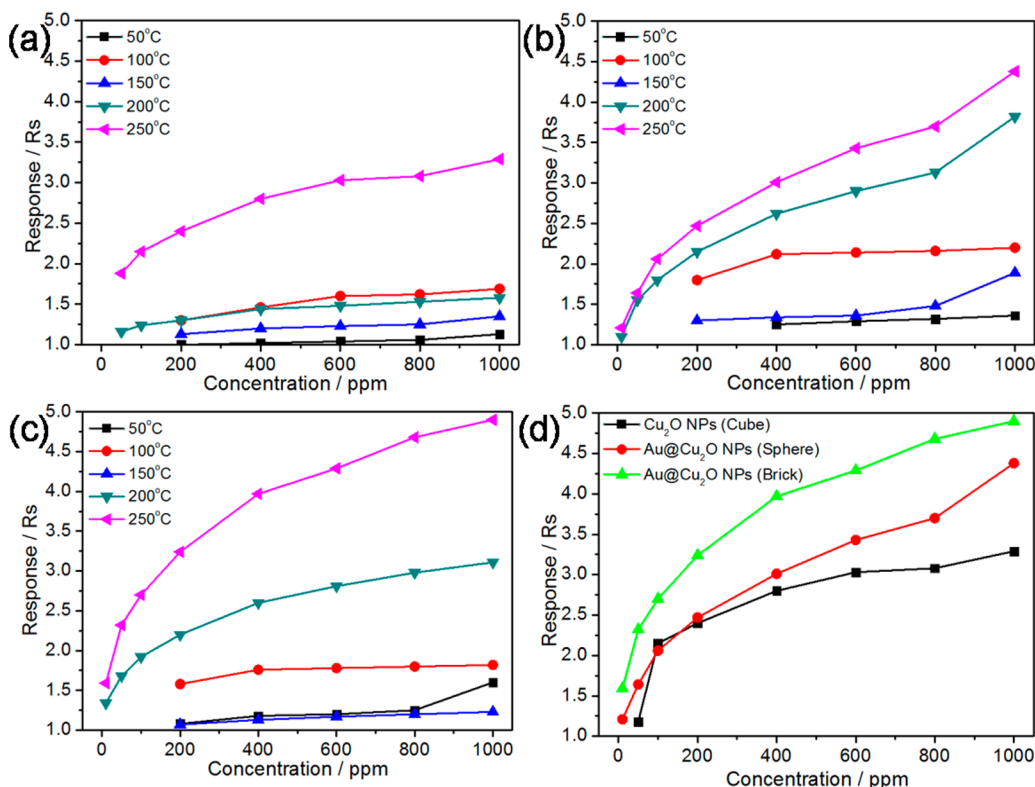
Figure 6. Response of as prepared sensing device at various temperatures for various CO concentrations: (a) Cu_2O NPs, (b) spherical $Au@Cu_2O$ core−shell, and (c) brick $Au@Cu_2O$ core−shell NPs. (d) Sensitivity of as prepared sensing device at 250 °C for various CO concentrations.

controlling mobile charge carriers. When Cu_2O sensor is exposed to air, oxygen molecules adsorb on the surface of the materials to form O^- ions by capturing electrons which generates holes, and therefore resistance decreases. In CO environments, CO gas reacts with the chemisorbed oxygen anions (eq 1).

$$2CO_{(gas)} + 2O_{(ads)}^- \rightarrow 2CO_{2(gas)} + 2e^- \qquad (1)$$
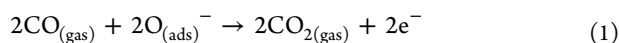
The red−ox reactions between CO and adsorbed surface oxygen release the electrons to the conduction band of Cu_2O, where recombination between the electrons and holes lowers carrier concentration and therefore resistance of Cu_2O increases. The significant variation in resistance can be attributed to the special structure advantages of the $Au@Cu_2O$ core−shell NPs. The low baseline resistance of $Au@Cu_2O$ compared to bare Cu_2O NPs above 150 °C can be explained on the basis of electronic sensitization of Au NRs.[19−21] The electronic sensitization of Au NRs results in the transfer of electron from conduction band of Cu_2O to Au NRs, because the Au work function (5.1 eV) is larger than that of Cu_2O (4.84 eV). Thus, the energy band bends higher at the Au/Cu_2O interface, which results in greater electron withdrawal and results in the increase in hole mobility.[40] A schematic illustration of charge transfer in Au/Cu_2O system is shown in Figure 7. Therefore, resistance of Cu_2O decreases with introduction of Au NPs above 100 °C. However, high resistance of brick shape $Au@Cu_2O$ core−shell NPs compared to cube shape Cu_2O below 100 °C suggests that electrons are the majority carrier at low temperature. Therefore, transfer of electron from Cu_2O to Au results in increase in resistance.[41] Furthermore, transition from p- to n-type response, at low operating temperature, is possibly related to the formation of an
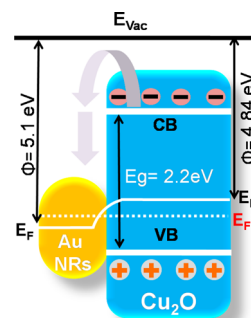

Figure 7. Schematic illustration of charge transfer in Au/Cu_2O system.

inversion layer type of mobile carrier at the surface. It has been reported that different gases has different contribution of surface electrons and holes in the overall conductivity, which leads for the predominating either p- or n-type response.[42]

The observed decrease in baseline resistance of Cu_2O with increasing temperatures is related to increase in carrier concentration, their mobility, and oxygen adsorption. It is possible that with increasing temperature electrons are excited to the conduction band, leaving holes in the valence band, and therefore conductivity increases. This hole mobility also increases with temperature as transport of carriers among the grains is directly related to temperature.[43] Furthermore, the oxygen chemisorption process is also accelerated as the temperature is raised.[44] Since Cu_2O is a p-type metal oxide, electron withdrawal from the conduction band of Cu_2O by oxygen molecules leads to an increment in hole mobility. Thus, the baseline resistance decreases with increasing temperature.

Furthermore, the lower baseline resistance of spherical shape $Au@Cu_2O$ core−shell NPs compared to other two structures is

7495

dx.doi.org/10.1021/am5008694 | ACS Appl. Mater. Interfaces 2014, 6, 7491−7497

related to their geometry which possibly affects the current flow. The electrical conductivity depends on both the density and the mobility of the charge carriers in a material. If we consider that the density and mobility of charge carrier is same in these devices then the mobility of the charge carriers depends on all inelastic scattering processes by which current flow is impeded. Therefore, the movement of an electric current in a material having grain boundaries is often far from the idealized picture under the influence of an applied electric field because of scattering of charge carriers at the interfaces between grains.[10,45,46] Therefore, the difference in baseline resistance of these NPs is possibly related to the arrangement of particles between two electrodes. A schematic presentation of flow of charge in sensing layer with their corresponding FESEM images is shown in Figure 8. The FESEM images are taken after
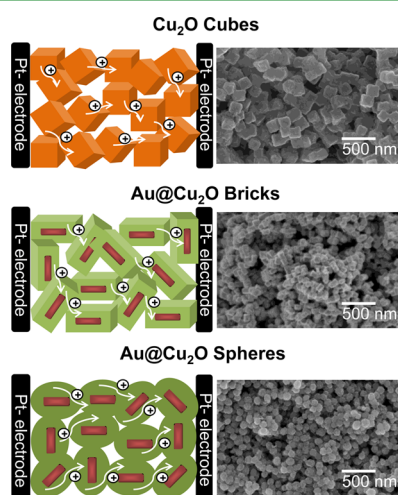
Figure 8. Schematic presentation of arrangement of particles between electrodes in sensing device along with their FESEM images.

heat treatment of the device at 300 °C, and they reveal no change in shape and size of sensing materials. It reveals that spherical shape Au@Cu_2O core−shell NPs is well-connected to each other due to spherical geometry which facilitates the charge flow. Compared to spherical shape Au@Cu_2O core−shell NPs, the cubic shape Cu_2O or brick shape Au@Cu_2O core−shell NPs are loosely connected to each other in sensing layer as shown in Figure 8. The presence of sharp edges in cube or brick like structure hinders the close contact between the particles, and therefore scattering of charge carriers at interfaces are larger in these structures. Therefore, baseline resistance of spherical shape Au@Cu_2O core−shell NPs is lower compared to other two structures.

CONCLUSIONS

Morphologically controlled Au@Cu_2O core−shell NPs were synthesized by simple solution route. The morphology of Au@Cu_2O core−shell NPs was tuned from brick to spherical shape by tuning the pH of the solution. The brick shape Au@Cu_2O core−shell NPs having length and width in range of 120 ± 10 and 50 ± 5 nm, respectively, were formed due to the epitaxial growth of {111} facets of Cu_2O over {111} planes of Au NRs. The decrease in pH of reaction medium resulted in the formation of spherical shape Au@Cu_2O core−shell NPs in a range of 100 ± 10 nm. In the absence of Au NRs, single crystalline cubelike Cu_2O NPs having 150−200 nm diameters

were formed. The sensor having Au@Cu_2O core−shell layer exhibited a higher sensitivity toward CO than that with bare Cu_2O NPs layer due to electronic sensitization of Au NRs. The maximum response of bare Cu_2O, brick, and spherical Au@Cu_2O core−shell NPs was 3.35, 5.67, and 4.38, respectively, at 250 °C for 1000 ppm of CO gas. Tuning the morphology of Au@Cu_2O core−shell NPs from brick to spherical shape facilitated the charge flow and significantly lowered the resistance. It was found that, below 150 °C, the inversion layer type of mobile carrier at the surface resulted in p- to n-type transition of response. It was successfully demonstrated that performance of sensor depends not only on the presence of Au NRs as catalyst but also on the morphology of the Au@Cu_2O core−shell NPs.

ASSOCIATED CONTENT

Ⓢ Supporting Information

XRD profile of as prepared Cu_2O and Au@Cu_2O core−shell NPs, UV−visible, spectra of Au NRs, Cu_2O, and Au@Cu_2O core−shell NPs, response transient of as prepared sensing devices at various temperatures, and response of as prepared sensing device at various temperatures for 1000 ppm of CO gas. This material is available free of charge via the Internet at http://pubs.acs.org.

AUTHOR INFORMATION

Corresponding Author
*E-mail: yeontae@jbnu.ac.kr. Tel: +82-63-270-2288. Fax: +82-63-270-2305.

Notes

The authors declare no competing financial interest.

ACKNOWLEDGMENTS

REFERENCES

(1) Milliron, D. J.; Hughes, S. M.; Cui, Y.; Manna, L.; Li, J.; Wang, L. W.; Alivisatos, A. P. Colloidal Nanocrystal Heterostructures with Linear and Branched Topology. *Nature* **2004**, *430*, 190−195.

(2) Martha, S.; Reddy, K. H.; Parida, K. M. Fabrication of In_2O_3 Modified ZnO for Enhancing Stability, Optical Behavior, Electronic Properties and Photocatalytic Activity for Hydrogen Production Under Visible Light. *J. Mater. Chem. A* **2014**, *2*, 3621−3631.

(3) Nashim, A.; Martha, S.; Parida, K. M. $Gd_2Ti_2O_7/In_2O_3$: Efficient Visible-Light-Driven Heterojunction-Based Composite Photocatlysts for Hydrogen Production. *ChemCatChem* **2013**, *5*, 2352−2359.

(4) Zhang, J.; Tang, Y.; Lee, K.; Ouyang, M. Nonepitaxial Growth of Hybrid Core−Shell Nanostructures with Large Lattice Mismatches. *Science* **2010**, *327*, 1634−1638.

(5) Reddy, K. H.; Parida, K. M. Fabrication, Characterization and Photoelectrochemical Properties of Cu-Doped $PbTiO_3$ and its Hydrogen Production Activity. *ChemCatChem* **2013**, *5*, 3812−3820.

(6) Peng, L.; Wei, Z.; Tong, W.; Qing, P.; Li, Y. Au-ZnO Hybrid Nanopyramids and Their Photocatalytic Properties. *J. Am. Chem. Soc.* **2011**, *133*, 5660−5663.

(7) Pany, S.; Naik, B.; Martha, S.; Parida, K. M. Plasmon Induced Nano Au Particle Decorated over S,N-Modified TiO_2 for Exceptional

Photocatalytic Hydrogen Evolution under Visible Light. *ACS Appl. Mater. Interfaces* **2014**, *6*, 839−846.

(8) Agarwala, S.; Lim, Z. H.; Nicholsan, E.; Ho, G. W. Probing the Morphology-Device Relation of Fe_2O_3 Nanostructures Towards Photovoltaic and Sensing Applications. *Nanoscale* **2012**, *4*, 194−205.

(9) Franke, M. E.; Koplin, T. J.; Simon, U. Metal and Metal Oxide Nanoparticles in Chemiresistors: Does the Nanoscale Matter? *Small* **2006**, *2*, 36−50.

(10) Rai, P.; Kwak, W.-K.; Yu, Y. T. Solvothermal Synthesis of ZnO Nanostructures and Their Morphology-Dependent Gas-Sensing Properties. *ACS Appl. Mater. Interfaces* **2013**, *5*, 3026−3032.

(11) Gurlo, A. Nanosensors: Towards Morphological Control of Gas Sensing Activity. SnO_2, In_2O_3, ZnO and WO_3 Case Studies. *Nanoscale* **2011**, *3*, 154−165.

(12) Williams, G.; Coles, G. S. V. Gas Sensing Properties of Nanocrystalline Metal Oxide Powders Produced by a Laser Evaporation Technique. *J. Mater. Chem.* **1998**, *8*, 1657−1664.

(13) Wang, C.; Yin, L.; Zhang, L.; Xiang, D.; Gao, R. Metal Oxide Gas Sensors: Sensitivity and Influencing Factors. *Sensors* **2010**, *10*, 2088−2106.

(14) Liu, X.; Zhang, J.; Guo, X.; Wang, S.; Wu, S. Core−Shell α-Fe_2O_3@SnO_2/Au Hybrid Structures and Their Enhanced Gas Sensing Properties. *RSC Adv.* **2012**, *2*, 1650−1655.

(15) Hwang, I. S.; Choi, J. K.; Woo, H. S.; Kim, S. J.; Jung, S.-Y.; Seong, T.-Y.; Kim, I.-D.; Lee, J. H. Facile Control of C_2H_5OH Sensing Characteristics by Decorating Discrete Ag Nanoclusters on SnO_2 Nanowire Networks. *ACS Appl. Mater. Interfaces* **2011**, *3*, 3140−3145.

(16) Ren, S.; Fan, G.; Qu, S.; Wang, Q. Enhanced H_2 Sensitivity at Room Temperature of ZnO Nanowires Functionalized by Pd Nanoparticles. *J. Appl. Phys.* **2011**, *110*, 084312.

(17) Arna, P. M.; Comotti, M.; Schüth, F. High-Temperature-Stable Catalysts by Hollow Sphere Encapsulation. *Angew. Chem., Int. Ed.* **2006**, *45*, 8224−8227.

(18) Subramanian, V.; Wolf, E. E.; Kamat, P. V. Influence of Metal/Metal Ion Concentration on the Photocatalytic Activity of TiO_2-Au Composite Nanoparticles. *Langmuir* **2003**, *19*, 469−474.

(19) Yu, Y. T.; Dutta, P. Examination of Au/SnO_2 Core-Shell Architecture Nanoparticle for Low Temperature Gas Sensing Applications. *Sens. Actuators, B* **2011**, *157*, 444−449.

(20) Yanagimoto, T.; Yu, Y. T.; Kenoko, K. Microstructure and CO Gas Sensing Property of Au/SnO_2 Core−Shell Structure Nanoparticles Synthesized by Precipitation Method and Microwave-Assisted Hydrothermal Synthesis Method. *Sens. Actuators, B* **2012**, *166−167*, 31−35.

(21) Kim, Y. S.; Rai, P.; Yu, Y. T. Microwave Assisted Hydrothermal Synthesis of Au@TiO_2 Core−Shell Nanoparticles for High Temperature CO Sensing Applications. *Sens. Actuators, B* **2013**, *186*, 633−639.

(22) Wu, R.-J.; Lin, D.-J.; Yu, M. R.; Chen, M. H.; Lai, H.-F. Ag@SnO_2 Core−Shell Material for Use in Fast-Response Ethanol Sensor at Room Operating Temperature. *Sens. Actuators, B* **2013**, *178*, 185−191.

(23) Wang, H.; Sun, Z.; Lu, Q.; Zeng, F.; Su, D. One-Pot Synthesis of (Au Nanorod)−(Metal Sulfide) Core−Shell Nanostructures with Enhanced Gas-Sensing Property. *Small* **2012**, *8*, 1167−1172.

(24) Wu, X. F.; Song, H. Y.; Yoon, J. M.; Yu, Y. T.; Chen, Y. F. Synthesis of Core-Shell Au@TiO_2 Nanoparticles with Truncated Wedge-Shaped Morphology and Their Photocatalytic Properties. *Langmuir* **2009**, *25*, 6438−6447.

(25) Zhang, Z.; Zhou, Y.; Zhang, Y.; Xiang, S.; Zhou, S.; Sheng, X. Encapsulation of Au Nanoparticles With Well-Crystallized Anatase TiO_2 Mesoporous Hollow Spheres for Increased Thermal Stability. *RSC Adv.* **2014**, *4*, 7313−7320.

(26) Tamaki, J.; Miyaji, A.; Makinodan, J.; Ogura, S.; Konishi, S. Effect of Micro-Gap Electrode on Detection of Dilute NO_2 Using WO_3 Thin Film Microsensors. *Sens. Actuators, B* **2005**, *108*, 202−206.

(27) Scott, R. W. J.; Yang, S. M.; Chabanis, G.; Coombs, N.; Williams, D. E.; Ozin, G. A. Tin Dioxide Opals and Inverted Opals: Near-Ideal Microstructures for Gas Sensors. *Adv. Mater.* **2001**, *13*, 1468−1472.

(28) Rai, P.; Yu, Y. T. Potential Barrier Modulation in ZnO Nanostructures and Their CO Sensing Properties. *Anal. Methods* **2013**, *5*, 4081−4087.

(29) Park, J. C.; Kim, J.; Kwon, H.; Song, H. Gram-Scale Synthesis of Cu_2O Nanocubes and Subsequent Oxidation to CuO Hollow Nanostructures for Lithium-Ion Battery Anode Materials. *Adv. Mater.* **2009**, *21*, 803−807.

(30) Hua, Q.; Shi, F.; Chen, K.; Chang, S.; Ma, Y.; Jiang, Z.; Pan, G.; Huang, W. Cu_2O−Au Nanocomposites with Novel Structures and Remarkable Chemisorption Capacity and Photocatalytic Activity. *Nano Res.* **2011**, *4*, 948−962.

(31) Won, Y. H.; Stanciu, L. A. Cu_2O and Au/Cu_2O Particles: Surface Properties and Applications in Glucose Sensing. *Sensors* **2012**, *12*, 13019−13033.

(32) Li, Q.; Xu, P.; Zhang, B.; Tsai, H.; Zheng, S.; Wu, G.; Wang, H.-L. Structure-Dependent Electrocatalytic Properties of Cu_2O Nanocrystals for Oxygen Reduction Reaction. *J. Phys. Chem. C* **2013**, *117*, 13872−13878.

(33) Zhang, J.; Liu, J.; Peng, Q.; Wang, X.; Li, Y. Nearly Monodisperse Cu_2O and CuO Nanospheres: Preparation and Applications for Sensitive Gas Sensors. *Chem. Mater.* **2006**, *18*, 867−871.

(34) Gou, X.; Wang, G.; Yang, J.; Park, J.; Wexler, D. Chemical Synthesis, Characterisation and Gas Sensing Performance of Copper Oxide Nanoribbons. *J. Mater. Chem.* **2008**, *18*, 965−969.

(35) Shishiyanu, S. T.; Shishiyanu, T. S.; Lupan, O. I.; Novel NO_2. Gas Sensor Based on Cuprous Oxide Thin films. *Sens. Actuators, B* **2006**, *113*, 468−476.

(36) Ho, J. Y.; Huang, M. H. Synthesis of Submicrometer-Sized Cu_2O Crystals with Morphological Evolution from Cubic to Hexapod Structures and Their Comparative Photocatalytic Activity. *J. Phys. Chem. C* **2009**, *113*, 14159−14164.

(37) Sau, T. K.; Murphy, C. J. Seeded High Yield Synthesis of Short Au Nanorods in Aqueous Solution. *Langmuir* **2004**, *20*, 6414−6420.

(38) Kuo, C. H.; Hua, T. E.; Huang, M. H. Au Nanocrystal-Directed Growth of Au−Cu_2O Core−Shell Heterostructures with Precise Morphological Control. *J. Am. Chem. Soc.* **2009**, *131*, 17871−17878.

(39) Huang, W.-C.; Lyu, L.-M.; Yang, Y.-C.; Huang, M. Synthesis of Cu_2O Nanocrystals from Cubic to Rhombic Dodecahedral Structures and Their Comparative Photocatalytic Activity. *J. Am. Chem. Soc.* **2012**, *134*, 1261−1267.

(40) Rai, P.; Khan, R.; Raj, S.; Majhi, S. M.; Park, K.-K.; Yu, Y.-T.; Lee, I.-H.; Sekhar, P. K. Au@Cu_2O Core-Shell nanoparticles as Chemiresistors for Gas Sensor Application: Effect of Potential Barrier Modulation on the Sensing Performance. *Nanoscale* **2014**, *6*, 581−588.

(41) Tan, Y.; Xue, X.; Peng, Q.; Zhao, H.; Wang, T.; Li, Y. Controllable Fabrication and Electrical Performance of Single Crystalline Cu_2O Nanowires with High Aspect Ratios. *Nano Lett.* **2007**, *7*, 3723−3728.

(42) Vallejos, S.; Stoycheva, T.; Umek, P.; Navio, C.; Snyders, R.; Bittencourt, C.; Llobet, E.; Blackman, C.; Moniz, S.; Correig, X. Au Nanoparticle-Functionalised WO_3 Nanoneedles and Their Application in High Sensitivity Gas Sensor Devices. *Chem.Commun.* **2011**, *47*, 565−567.

(43) Yamazoe, N.; Shimanoe, K.; Sawada, C. Contribution of Electron Tunneling Transport in Semiconductor Gas Sensor. *Thin Solid Films* **2007**, *515*, 8302−8309.

(44) Zhang, G.; Liu, M. Effect of Particle Size and Dopant on Properties of SnO_2-Based Gas Sensors. *Sens. Actuators, B* **2000**, *69*, 144−152.

(45) Ramirez, F. H.; Prades, J. D.; Diaz, R. J.; Fischer, T.; Rodriguez, A. R.; Mathur, S.; Morante, J. R. On the Role of Individual Metal Oxide Nanowires in the Scaling Down of Chemical Sensors. *Phys. Chem. Chem. Phys.* **2009**, *11*, 7105−7110.

(46) Volanti, D. P.; Felix, A. A.; Orlandi, M. O.; Whitfield, G.; Yang, D.-J.; Longo, E.; Tuller, H. L.; Varela, J. A. The Role of Hierarchical Morphologies in the Superior Gas Sensing Performance of CuO-Based Chemiresistors. *Adv. Funct. Mater.* **2013**, *23*, 1759−1766.